



Research Article

Superior high-temperature wear resistance of an Ir-Ta-Ni-Nb bulk metallic glass



Fei Sun^a, Shengtao Deng^a, Jianan Fu^b, Jiahua Zhu^a, Dandan Liang^c, Pengfei Wang^a, Hang Zhao^a, Feng Gong^a, Jiang Ma^{a,*}, Yanhui Liu^{d,*}, Jun Shen^a

^a Shenzhen Key Laboratory of High Performance Nontraditional Manufacturing, College of Mechatronics and Control Engineering, Shenzhen University, Shenzhen 518060, China

^b Shenzhen Key Laboratory of Cross-scale Manufacturing Mechanics Southern University of Science and Technology, Shenzhen 518055, China

^c Shanghai Engineering Research Center of Physical Vapor Deposition (PVD) Superhard Coating and Equipment, Shanghai Institute of Technology, Shanghai 201418, China

^d Institute of Physics, Chinese Academy of Sciences, Beijing 100190, China

ARTICLE INFO

Article history:

Received 18 January 2023

Revised 12 February 2023

Accepted 13 February 2023

Available online 7 April 2023

Keywords:

High-temperature alloy

Superior wear resistance

Wear mechanisms

Bulk metallic glass

ABSTRACT

Wear resistance is a critical consideration in engineering applications. In this study, we demonstrated an Ir-Ta-Ni-Nb bulk metallic glass (BMG) with outstanding high-temperature wear resistance and revealed its promising applications in extreme environments. The wear behavior and mechanism were systematically investigated from room temperature (RT) to 750 °C. The results show that the wear rate increases from $\sim 2.65 \times 10^{-6} \text{ mm}^3 \text{ N}^{-1} \text{ m}^{-1}$ to $\sim 10.56 \times 10^{-6} \text{ mm}^3 \text{ N}^{-1} \text{ m}^{-1}$ in the temperature span RT to 400 °C, following abrasive wear and flash temperature-induced oxidative wear during the friction. However, at the higher temperature of 600 °C, further heating due to frictional heat leads to a softening of the wear surface, resulting in a maximum wear rate of $\sim 20.99 \times 10^{-6} \text{ mm}^3 \text{ N}^{-1} \text{ m}^{-1}$ under softness-driven abrasive wear as well as oxidative wear. Interestingly, the wear resistance at an even higher temperature of 750 °C shows a paradoxical improvement of $\sim 7.08 \times 10^{-6} \text{ mm}^3 \text{ N}^{-1} \text{ m}^{-1}$, which is attributed to the formation of an oxide layer with a thickness of several microns, avoiding violent wear of BMG. The results demonstrate the unreported outstanding high-temperature wear resistance of the Ir-Ta-Ni-Nb BMG, especially its excellent capability to resist wear at 750 °C, leading to the promising applications of BMG in the fields of aerospace, metallurgy, and nuclear industries.

© 2023 Published by Elsevier Ltd on behalf of The editorial office of Journal of Materials Science & Technology.

1. Introduction

In practical applications, friction between parts is inevitable, and excessive wear leads to the failure of the equipment [1,2]. Therefore, the capability to resist wear and tear, especially in extreme environments, such as high temperatures, is one of the most important indicators when assessing the suitability of materials [3]. Typical materials such as tungsten carbide, silicon carbide, and diamond are considered to exhibit the most excellent wear resistance due to their ultra-high hardness [4,5]. However, the high hardness and wear resistance of the material appear to be mutually exclusive with machinability. The high hardness ensures excellent wear resistance but results in huge processing costs and technical troubles for its manufacture, especially for micro-fabrication and precision manufacturing [6,7]. Therefore, materials

that combine excellent wear resistance and high machinability are extremely desirable in precision manufacturing fields, such as glass molding, medical devices, and aerospace.

Metallic glass (MG), which was first developed in the 1960s, shows high strength, high hardness, and excellent wear resistance compared with its corresponding crystalline alloys [8–11]. MG is prepared by rapid cooling technology, which preserves its liquid-like atomic structure. This unique atomic structure endows MG with excellent mechanical and chemical properties and confers excellent processability [12–15]. The superior processability of MG is attributed to its glassy atomic structure, which provides excellent fluidity in a temperature span known as the supercooled liquid region (SLR) [16,17]. Utilizing the thermoplastic forming (TPF) method, MG can be processed into complex and precise structures such as nanowires, gratings, and microlens arrays [14,18,19]. In addition to this, MGs also perform well on wear resistance due to their unique amorphous structures [14]. To date, extensive work has investigated the wear behavior and mechanism of

* Corresponding authors.

E-mail addresses: majiang@szu.edu.cn (J. Ma), yanhui.liu@iphy.ac.cn (Y. Liu).

different systems of MG, such as Ti-, Fe-, Zr-, Al-, Mg-, and Co-based, which systematically demonstrate their superior wear resistance to the corresponding alloys [20–29]. However, the wear behavior and applications of MG at higher temperatures (above 600 °C) have rarely been reported due to the relatively low glass transition temperature (T_g) of conventional MG systems. In 2019, Liu and co-workers [30] developed a novel Ta-based (Ir-Ta-Ni-(B)) high-temperature bulk MG (BMG) system with unprecedentedly excellent high-temperature performance guided by the high throughput strategy. The ultra-high strength (~ 5.1 GPa), ultra-high T_g (~ 830 °C), and ultra-wide SLR (~ 136 °C) endow this BMG system with an attractive prospect for widespread engineering applications. To date, studies on the tribological behavior of the above-mentioned Ta-based BMG have not been reported. Therefore, a systematic investigation of the wear behavior and mechanism of this BMG in the ambient to the high-temperature environment has both engineering significance and research interest.

In this work, the wear behavior and mechanism of a novel Ta-based BMG (Ir_{29.8}Ta_{34.6}Ni_{29.3}Nb_{6.3}, which was developed based on the Ir-Ta-Ni-(B)) at room temperature (RT) to 750 °C was systematically investigated. The results show that the Ir-Ta-Ni-Nb BMG exhibits superior wear resistance compared with other typical MG systems throughout the temperature range. The wear rates of Ir-Ta-Ni-Nb BMG at RT, 200 °C, 400 °C, 600 °C, and 750 °C were calculated as 2.65×10^{-6} mm³ N⁻¹ m⁻¹, 7.52×10^{-6} mm³ N⁻¹ m⁻¹, 10.59×10^{-6} mm³ N⁻¹ m⁻¹, 20.99×10^{-6} mm³ N⁻¹ m⁻¹, and 7.08×10^{-6} mm³ N⁻¹ m⁻¹, respectively. For comparison, a typical Zr-based BMG (Zr₅₅Cu₃₀Al₁₀Ni₅) developed by Inoue et al. [31] was chosen for tribological experiments at RT and 200 °C. The wear rates of Zr₅₅Cu₃₀Al₁₀Ni₅ at RT, 200 °C were calculated as 83.24×10^{-6} mm³ N⁻¹ m⁻¹, 172.16×10^{-6} mm³ N⁻¹ m⁻¹, respectively. Our results demonstrate that the Ir-Ta-Ni-Nb BMG exhibits

remarkably superior wear resistance compared with other reported MG systems throughout RT to 750 °C, elucidating its widespread application in precision instruments and harsh environments.

2. Experimental

2.1. Sample preparation

The nominal composition of Ir_{29.8}Ta_{34.6}Ni_{29.3}Nb_{6.3} BMG was prepared using copper mold casting. The alloy ingots were prepared by arc melting a mixture of elements with a purity of at least 99.9% under a Ti-purified Ar atmosphere. Each ingot was remelted five times to ensure a homogeneous composition. BMG plates with a dimension of 1.2 mm × 12 mm × 15 mm were obtained by casting the molten alloy into a copper die. For comparison, a classic Zr-based (Zr₅₅Cu₃₀Al₁₀Ni₅) BMG was cast by using the same method. The above-mentioned Ta-based and Zr-based BMGs were cut into 10 mm diameter disks (shown in Fig. 1(b)) by using low-speed wire electrical discharge machining (WEDM; SODICK AP250L). Prior to friction experiments and performance characterization, all samples were ground with 800 to 2000 grit sandpaper and then polished to mirror level by using 0.1 μm diamond abrasive fluids.

2.2. Microstructure characterizations

The glassy nature of the samples was confirmed by X-ray diffraction (XRD; Rigaku MiniFlex 600) with Cu K_α radiation. The thermal properties of BMG samples were measured by differential scanning calorimetry (DSC; Perkin-Elmer DSC-8000) at a heating rate of 20 K min⁻¹. The micromorphology and elemental distributions of the samples were characterized by using field scanning

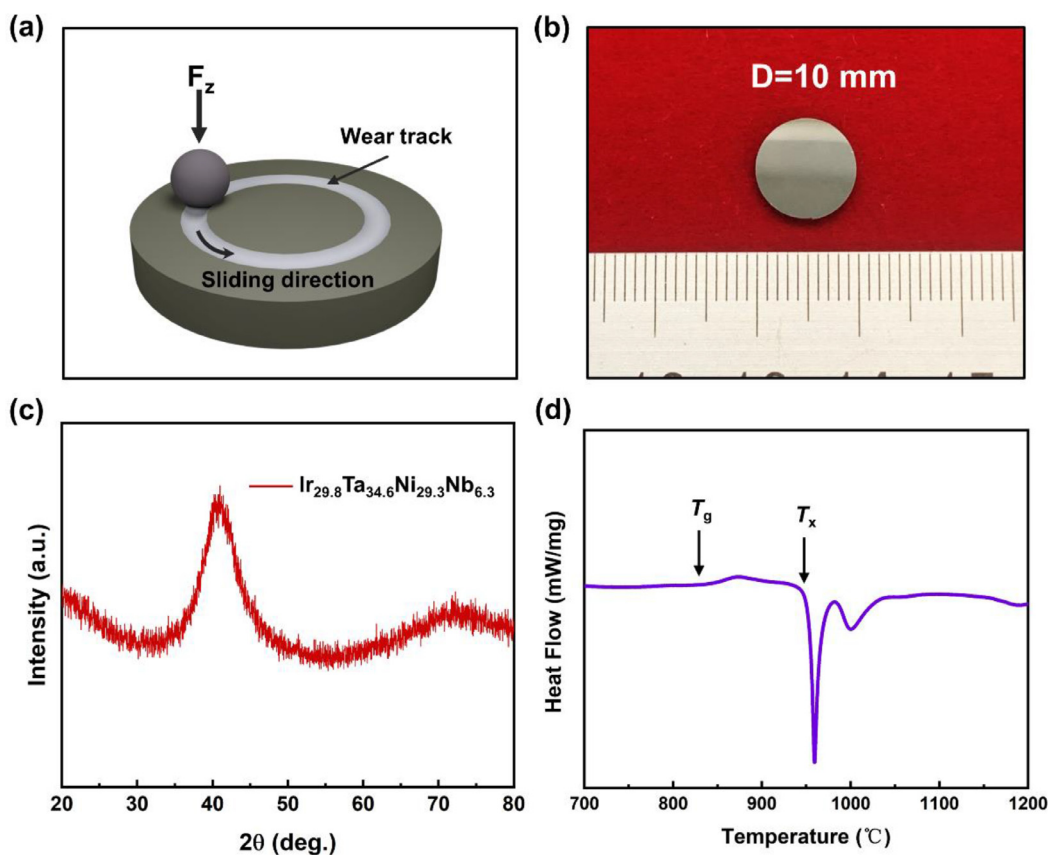


Fig. 1. (a) Schematic of wear test. (b) Optical photograph of the BMG sample before the wear experiment. (c, d) XRD and DSC curves of the Ir_{29.8}Ta_{34.6}Ni_{29.3}Nb_{6.3} BMG.

electron microscopy (SEM, FEI QUANTA FEG 450) equipped with energy disperse spectroscopy (EDS). The atomic structure was characterized by transmission electron microscopy (TEM; JEM-2100F) and the TEM samples were prepared on an FEI Scios SEM/FIB dual beam system. The hardness and modulus of the BMG samples were tested by using a nanoindenter (TI750 Hysitron Ltd.). Ten points per sample were tested to ensure the reliability of the data. The maximum load was 100 mN and the loading rate was $2500 \mu\text{N s}^{-1}$.

2.3. Tribological testing

Dry sliding wear tests were performed on the top surface of the BMG samples using a ball-on-disk wear machine (Rtec MFT-5000, USA) under an air atmosphere, the schematic is depicted in Fig. 1(a). A commercial zirconium dioxide (ZrO_2) ball (9.5 mm diameter) with a hardness of ~ 14 GPa was chosen as the counterpart. A fixed sliding speed of 300 r min^{-1} , a total sliding time of 15 min, and a load of 30 N were applied to all wear tests. To investigate the wear performance of Ta-based BMG at high temperatures, the temperatures were set to RT, 200 °C, 400 °C, 600 °C, and 750 °C, respectively. Since the relatively low T_g of Zr-based BMG, the wear temperature was set to RT and 200 °C. The 3D morphology and wear volume of the wear tracks were evaluated with a white light interferometer (Bruker ContourGT-X 3D). All the samples were ultrasonically cleaned with alcohol and deionized water prior to evaluation. The wear rate (ω) of the samples experimented with different parameters was calculated by using the following equation:

$$\omega = \frac{V_{\text{loss}}}{F * L}, \quad (1)$$

where V_{loss} is the wear volume loss (mm^3), L is the sliding distance (m), and F is the applied normal load (N).

3. Results and discussion

The XRD result of the $\text{Ir}_{29.8}\text{Ta}_{34.6}\text{Ni}_{29.3}\text{Nb}_{6.3}$ BMG is presented in Fig. 1(c). A broad diffraction peak can be found at about 42° , which confirms its fully glassy nature. Fig. 1(d) presents the DSC results of the $\text{Ir}_{29.8}\text{Ta}_{34.6}\text{Ni}_{29.3}\text{Nb}_{6.3}$ BMG, where its T_g is about 827 °C, T_x is about 955 °C, and ΔT is about 128 °C. Accordingly, we confirmed

the glassy nature and thermal properties of the $\text{Zr}_{55}\text{Cu}_{30}\text{Al}_{10}\text{Ni}_5$ BMG (presented in Figs. S1 and S2 in the Supplementary Material). T_g is about 420 °C, T_x is about 480 °C, and ΔT is about 60 °C, which is consistent with Ref. [18]. In addition, the average hardness and modulus calculated from nanoindentation were 6.40 GPa and 112.21 GPa (Fig. S3), respectively.

3.1. Wear behavior at RT

Fig. 2(a, d) displays the coefficient of friction (COF) depending on the time of Ir-Ta-Ni-Nb and Zr-Cu-Ni-Al BMG at RT, respectively. The COF of the two samples exhibits an abrupt rise followed by a gradual fall, which is known as the “running-in” stage associated with the roughness of the contacted and loaded surface [32]. It is noticeable that Ta-based BMGs undergo a longer “running-in” state than Zr-based ones, which can be attributed to the higher hardness of the former. In the subsequent “stable-wear” stage, the average COF of the Ta-based sample is about 0.50, and relatively stable overall. Accordingly, the average COF of the Zr-based one is approximately 0.55 and several mutations can be observed. The presence of fluctuations in Zr-based samples indicates the occurrence of cracking or peeling [27], which indicates that the Zr-based BMG is more susceptible to wear than the Ta-based BMG under the same wear conditions, that is, the Ta-based BMG exhibits superior wear resistance. Fig. 2(b, e) compares the 3D morphology of Ta- and Zr-based BMG wear traces. The wear of Ta-based BMG is extremely slight, whereas the wear of Zr-based BMG is relatively intense. The depths of the wear traces are 2.1 μm ($d_{\text{Max}1}$) and 17.4 μm ($d_{\text{Max}2}$) in accordance with the cross-sectional profiles presented in Fig. 2(c, f). The area of the wear profile is 358 μm^2 (S_1) for Ta-based BMG and 11,237 μm^2 (S_2) for Zr-based BMG by using the integral method. The wear volumes (V_{loss}) for Ta- and Zr-based BMG are $\sim 6.74 \times 10^{-3}$ and $\sim 211.71 \times 10^{-3} \text{ mm}^3$ by integrating over the entire wear trail, respectively. In accordance with Eq. (1), the wear rate (ω) of Ta- and Zr-based BMG at RT is $\sim 2.65 \times 10^{-6} \text{ mm}^3 \text{ N}^{-1} \text{ m}^{-1}$ (ω_1) and $\sim 83.24 \times 10^{-6} \text{ mm}^3 \text{ N}^{-1} \text{ m}^{-1}$ (ω_2), respectively. In summary, the wear resistance of $\text{Ir}_{29.8}\text{Ta}_{34.6}\text{Ni}_{29.3}\text{Nb}_{6.3}$ BMG is remarkably better than that of $\text{Zr}_{55}\text{Cu}_{30}\text{Al}_{10}\text{Ni}_5$ at RT.

To investigate the wear mechanism of the two abovementioned BMGs at RT, we examined the wear traces using SEM and EDS. As shown in Fig. 3(a), the surface of the Ta-based BMG is relatively smooth and grooves can be observed, which implies the

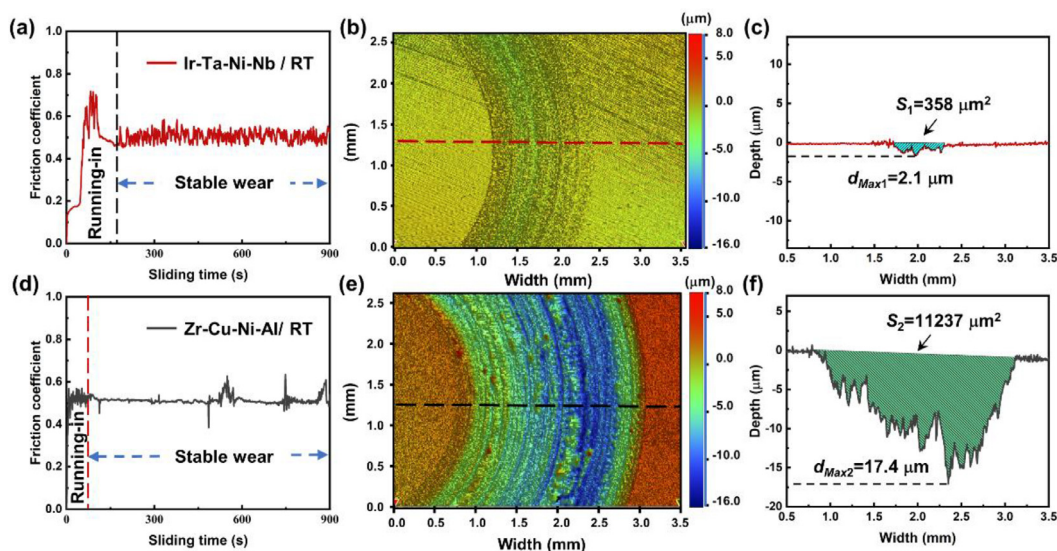


Fig. 2. (a) COF depending on the time of Ta-based BMG at RT. (b) Wear morphology of Ta-based BMG at RT. (c) Cross-sectional profile of Ta-based BMG's wear traces. (d) COF depending on the time of Zr-based BMG at RT. (e) Wear morphology of Zr-based BMG at RT. (f) Cross-sectional profile of Zr-based BMG's wear traces.

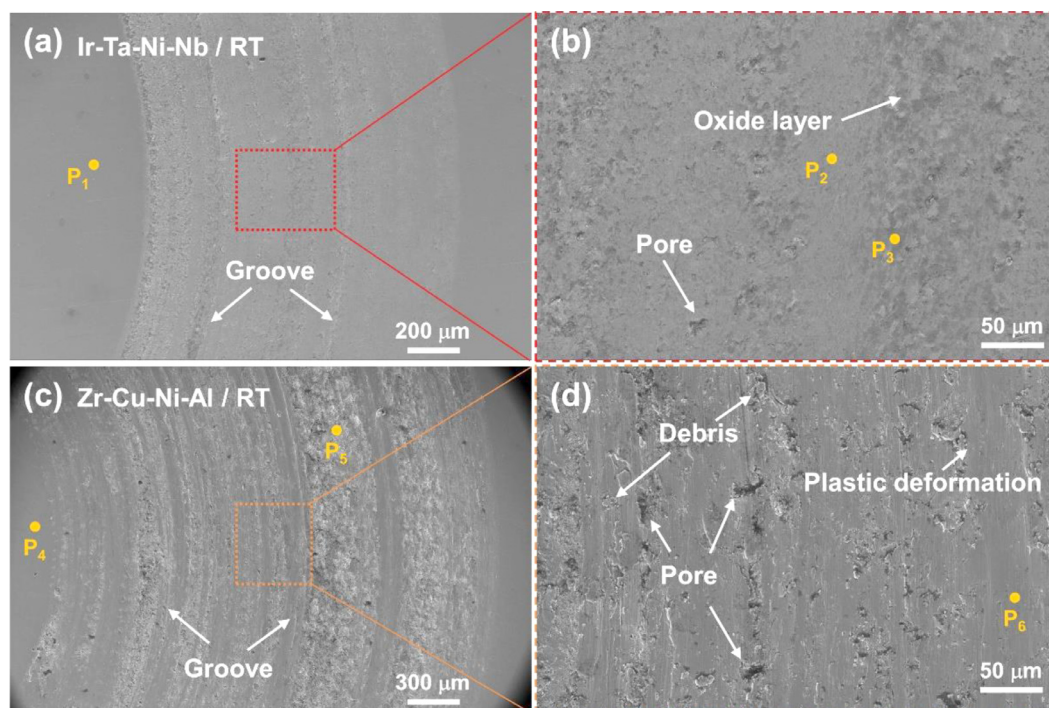


Fig. 3. (a, b) Wear morphology and elemental analysis of Ir-Ta-Ni-Nb BMG at RT. (c, d) Wear morphology and elemental analysis of Zr-Cu-Ni-Al BMG at RT.

Table 1

Summary of the elemental distribution of Ir-Ta-Ni-Nb and Zr-Cu-Ni-Al wear samples at RT.

Point No.	Element Content (at.%)								
	Ir	Ta	Ni	Nb	O	Zr	Cu	Ni	Al
P ₁	28.64	34.42	27.30	6.69	2.96	0.00	⊗	⊗	⊗
P ₂	25.41	25.43	24.69	3.23	21.23	0.00	⊗	⊗	⊗
P ₃	15.56	15.47	14.64	1.80	52.53	0.00	⊗	⊗	⊗
P ₄	⊗	⊗	⊗	⊗	3.67	48.75	20.14	14.90	12.54
P ₅	⊗	⊗	⊗	⊗	50.25	15.19	6.93	4.95	22.68
P ₆	⊗	⊗	⊗	⊗	24.46	27.38	12.44	9.15	26.58

occurrence of slight abrasive wear [20]. In the enlarged image (Fig. 3(b)), fewer pores can be observed, indicating slight fatigue wear. Obvious oxidation can also be found (the darker areas). The elemental distribution of the non-wear area (P₁), grooves (P₂), and the oxide layer (P₃) was examined to further study the mechanism of wear, as summarized in Table 1. The oxygen content is 2.96% in the non-worn area, 21.23% in the furrow, and up to 52.53% in the oxide layer. No Zr element was detected in the three regions, which proves that no adhesion occurs from the counterpart material. Oxidative wear occurred on the surface due to the inevitable heating up during the friction process [33]. The surface inside the furrow, which is considered to be a fresher layer, contains less oxygen than the oxide layer [34]. In summary, the wear mechanisms of Ir_{29.8}Ta_{34.6}Ni_{29.3}Nb_{6.3} BMG at RT are oxidative wear, abrasive wear, and minor fatigue wear. By contrast, the Zr-based BMG underwent more severe wear, which can be demonstrated by the rougher surface, deeper grooves, and wider wear traces shown in Fig. 3(c). In the magnified view (Fig. 3(d)), the adhesion of debris, more severe porosity, and remarkably plastic deformation can be observed, indicating the occurrence of severe abrasive wear, fatigue wear, and adhesive wear. In addition, the distribution of elements in different characteristic regions of the Zr-based BMG was examined by using EDS. As shown in Table 1, the oxygen content of P₅ and P₆ is 50.25% and 24.26% respectively, indicating the occurrence of oxidative wear. Therefore, the wear mechanism of Zr₅₅Cu₃₀Al₁₀Ni₅ BMG at RT is a combination of more severe abrasive wear, fatigue wear, adhesive wear, and oxidative wear.

3.2. Wear behavior at 200 °C

Fig. 4(a, d) compares the COF of Ir_{29.8}Ta_{34.6}Ni_{29.3}Nb_{6.3} and Zr₅₅Cu₃₀Al₁₀Ni₅ BMGs at 200 °C. Compared with the results at RT, the characteristics of the COF at 200 °C can be summarized as follows: (1) The Ta-based BMG undergoes a shorter “running-in” stage, and minor fluctuations in the “stable wear” stage can be observed. (2) The Zr-based BMG shows mostly no “running-in” stage and more dramatic fluctuations in the “stable wear” stage. The shorter “running-in” period can be attributed to a reduction in hardness due to increased temperature. Fig. 4(b, c) presents the 3D appearance of wear trace (Ta-based BMG) at 200 °C and its cross-sectional profile, which can be noticed as an increase in wear compared with RT. The maximum depth of the wear trace is 2.9 μm (d_{Max3}) and the cross-sectional area obtained by integration is ~1015 μm² (S_3). Correspondingly, the shape of the wear trace (Zr-based BMG) and its cross-sectional profile are shown in Fig. 4(e, f). The maximum depth of the wear trace is 28.6 μm (d_{Max4}) and the cross-sectional area obtained by integration is ~23,242 μm² (S_4). According to Eq. (1), the wear rate (ω) of Ta- and Zr-based BMGs at 200 °C is $\sim 7.52 \times 10^{-6} \text{ mm}^3 \text{ N}^{-1} \text{ m}^{-1}$ (ω_3) and $\sim 172.16 \times 10^{-6} \text{ mm}^3 \text{ N}^{-1} \text{ m}^{-1}$ (ω_4), respectively.

Fig. 5(a) shows the SEM image of the wear trace (Ta-based BMG) at 200 °C. We can detect the presence of slight grooves, which are considered to be evidence of abrasive wear. Different from the wear appearance at RT, the wear trace at 200 °C contains a large amount of “white powders”. In the magnified view

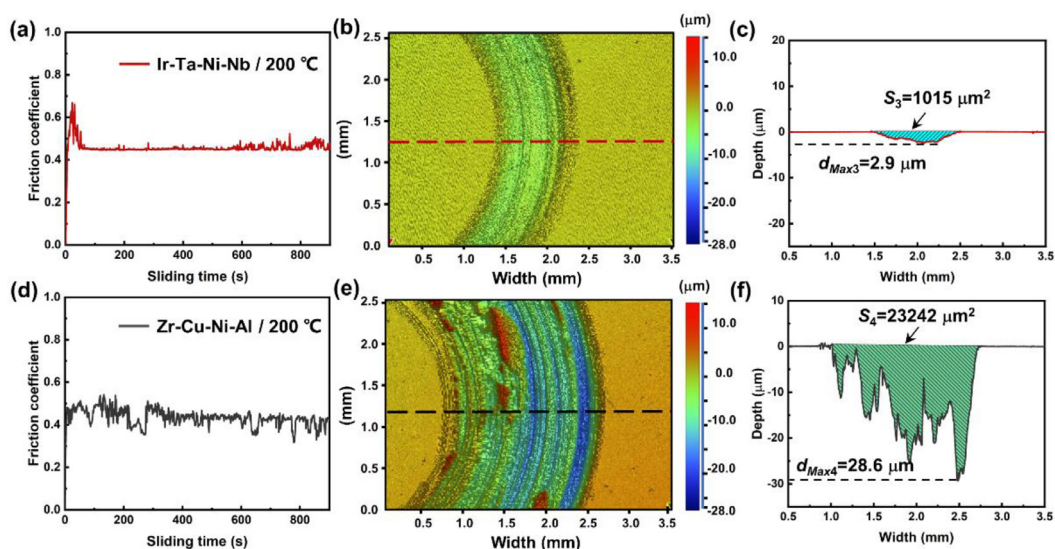


Fig. 4. (a) COF depending on the time of Ta-based BMG at 200 °C. (b) Wear morphology of Ta-based BMG at 200 °C. (c) Cross-sectional profile of Ta-based BMG’s wear trace. (d) COF depending on the time of Zr-based BMG at 200 °C. (e) Wear morphology of Ta-based BMG at 200 °C. (f) Cross-sectional profile of Zr-based BMG’s wear trace.

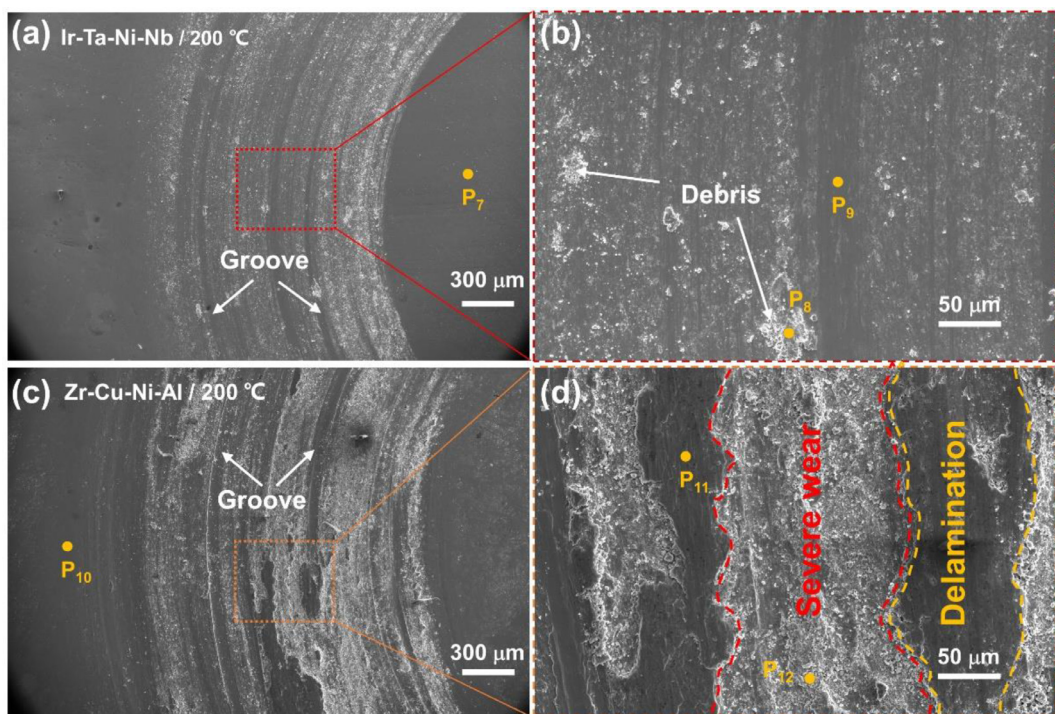


Fig. 5. (a, b) Wear morphology and elemental analysis of Ir-Ta-Ni-Nb BMG at 200 °C. (c, d) Wear morphology and elemental analysis of Zr-Cu-Ni-Al BMG at 200 °C.

(Fig. 5(b)), the “white powders” can be identified as the adhesion of numerous oxide particles. To further confirm the wear mechanism, the elemental distributions of non-wear areas (P_7), oxide particles (P_8), and grooves (P_9) were examined. As summarized in Table 2, the oxygen contents of the non-wear area, oxide particles, and grooves are 3.45%, 53.79%, and 35.73%, respectively. On the basis of these results, the wear mechanism of Ta-based MG at 200 °C is a combination of oxidative wear, adhesive wear, and slight abrasive wear. Correspondingly, the wear morphology of Zr-based BMG at 200 °C is shown in Fig. 5(c). Severe furrow and delamination on the surface of the wear trace indicate that the Zr-based BMG underwent severe wear at 200 °C. In the enlarged view (Fig. 5(d)), remarkably peeling and delamination can be observed, which indicates the occurrence of severe fatigue wear. The distribution of

elements in the non-wear area (P_{10}), delaminated area (P_{10}), and peeled area (P_{11}) is summarized in Table 2. The oxygen content in the peeled and delaminated areas is 49.76% and 55.67%, respectively. The oxygen content in the non-wear area is merely 3.03%, which means that the temperature rise due to the flash temperature leads to violent oxidation dominating the wear process. In conclusion, the wear mechanism of $Zr_{55}Cu_{30}Al_{10}Ni_5$ BMG at 200 °C is a combination of severe oxidative wear, fatigue wear, and abrasive wear.

3.3. Wear behavior at 400–750 °C

The wear behavior of $Ir_{29.8}Ta_{34.6}Ni_{29.3}Nb_{6.3}$ BMG at higher temperatures is discussed separately due to the severe wear of

Table 2
Summary of the elemental distribution of Ir-Ta-Ni-Nb and Zr-Cu-Ni-Al wear samples at 200 °C.

Point No.	Element Content (at.%)								
	Ir	Ta	Ni	Nb	O	Zr	Cu	Ni	Al
P ₇	29.04	32.70	28.84	5.98	3.45	0.00	⊗	⊗	⊗
P ₈	15.41	14.83	14.43	1.54	53.79	0.00	⊗	⊗	⊗
P ₉	20.52	21.16	20.58	2.01	35.73	0.00	⊗	⊗	⊗
P ₁₀	⊗	⊗	⊗	⊗	3.03	49.41	30.44	4.70	12.42
P ₁₁	⊗	⊗	⊗	⊗	49.76	12.11	5.24	3.75	29.13
P ₁₂	⊗	⊗	⊗	⊗	55.67	14.95	5.57	4.05	19.76

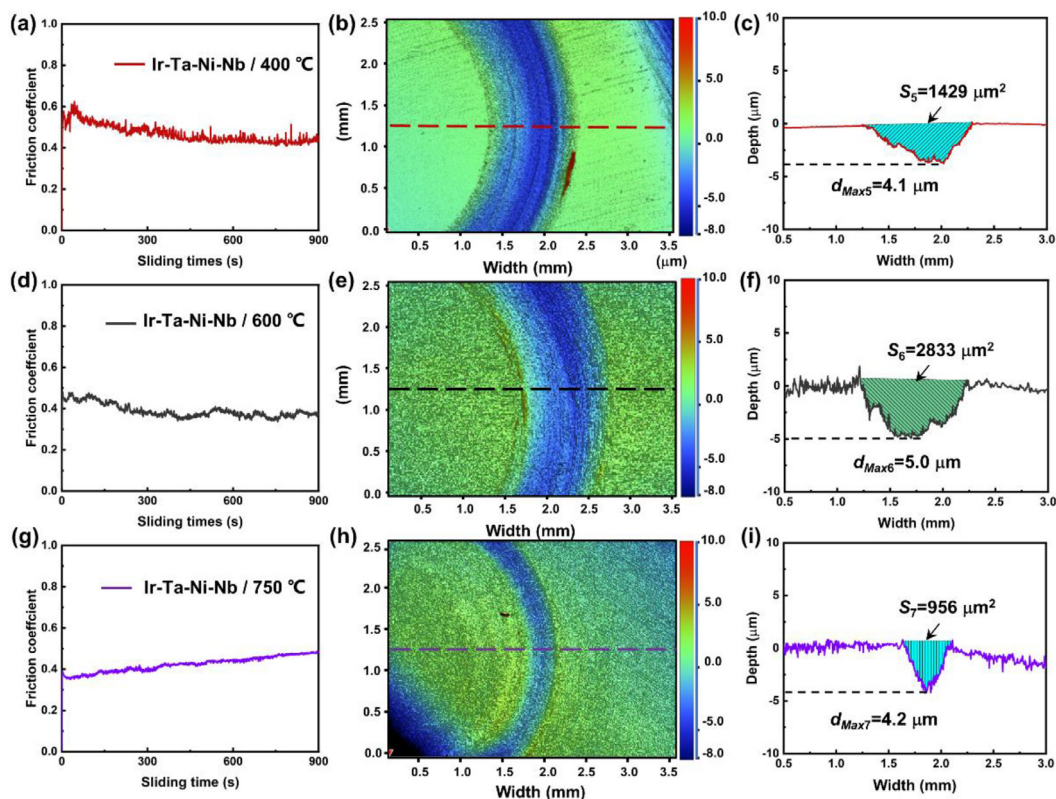


Fig. 6. (a) Friction coefficient of Ta-based BMG at 400 °C. (b) Wear morphology of Ta-based BMG at 400 °C. (c) Cross-sectional profile of wear trace 400 °C. (d) Friction coefficient of Ta-based BMG at 600 °C. (e) Wear morphology of Ta-based BMG at 600 °C. (f) Cross-sectional profile of wear trace at 600 °C. (g) Friction coefficient of Ta-based BMG at 750 °C. (h) Wear morphology of Ta-based BMG at 750 °C. (i) Cross-sectional profile of wear trace at 750 °C.

Zr₅₅Cu₃₀Al₁₀Ni₅ BMG at 200 °C. Fig. 6(a) presents the COF results of Ta-based BMG at 400 °C. The COF enters the “stable-wear” stage after a short “running-in” stage. Small fluctuations and a gradual downward trend can also be observed. Fig. 6(b, c) shows the corresponding 3D shape and cross-sectional profile of the wear traces, where the wear volume and depth increase with the increased temperature. The maximum depth of wear trace is 4.1 μm (d_{Max5}), and the cross-sectional area is $\sim 1429 \mu\text{m}^2$ (S_5). Hence, the wear rate of Ta-based BMG at 400 °C is calculated to be $\sim 10.59 \times 10^{-6} \text{ mm}^3 \text{ N}^{-1} \text{ m}^{-1}$ (ω_5). The COF of Ta-based BMG at 600 °C is displayed in Fig. 6(d). With the increase in temperature, the hardness of the BMG decreases, and the “running-in” stage cannot be observed. In the “stable wear” stage, the COF decreases gradually, which is similar to the results at 400 °C and can be attributed to the lubrication of the oxide film [35]. Greater fluctuations can be found at 400 °C, which may be due to the peeling or cracking at higher temperatures. Fig. 6(e, f) provides the 3D shape and cross-sectional profile of the wear trace at 600 °C. The maximum depth of the wear trace is 5.0 μm (d_{Max6}), and the wear volume is $2833 \mu\text{m}^2$ (S_6), which gives a corresponding wear rate

of $20.99 \times 10^{-6} \text{ mm}^3 \text{ N}^{-1} \text{ m}^{-1}$ (ω_6) in accordance with Eq. (1). Wear experiments were conducted at 750 °C, which is extremely close to T_g , to investigate the wear resistance of Ta-based BMG under extreme conditions. The COF of Ta-based BMG at 750 °C is illustrated in Fig. 6(g). Interestingly, the COF at 750 °C exhibits some features that are distinguished from lower temperatures: (1) The tendency of COF is to gradually increase rather than gradually decrease. (2) In the “stable-wear” stage, few fluctuations can be observed. These features indicate a transformation of the main wear mechanisms, which will be discussed in subsequent chapters. Fig. 6(h, i) presents the 3D shape and cross-sectional profile of the wear trace at 750 °C. The degree of wear decreases with increasing temperatures up to 750 °C. The maximum depth of the wear trace is 4.2 μm (d_{Max7}) and the cross-sectional area is $\sim 956 \mu\text{m}^2$ (S_7). When temperature increases from 600 °C to 750 °C, the wear rate paradoxically decreases from $\sim 20.99 \times 10^{-6} \text{ mm}^3 \text{ N}^{-1} \text{ m}^{-1}$ to $\sim 7.08 \times 10^{-6} \text{ mm}^3 \text{ N}^{-1} \text{ m}^{-1}$, which further validates the transformation of the wear mechanism.

The SEM morphology of the wear trace at 400 °C is illustrated in Fig. 7(a). Slight grooves and areas of visible “white powders”

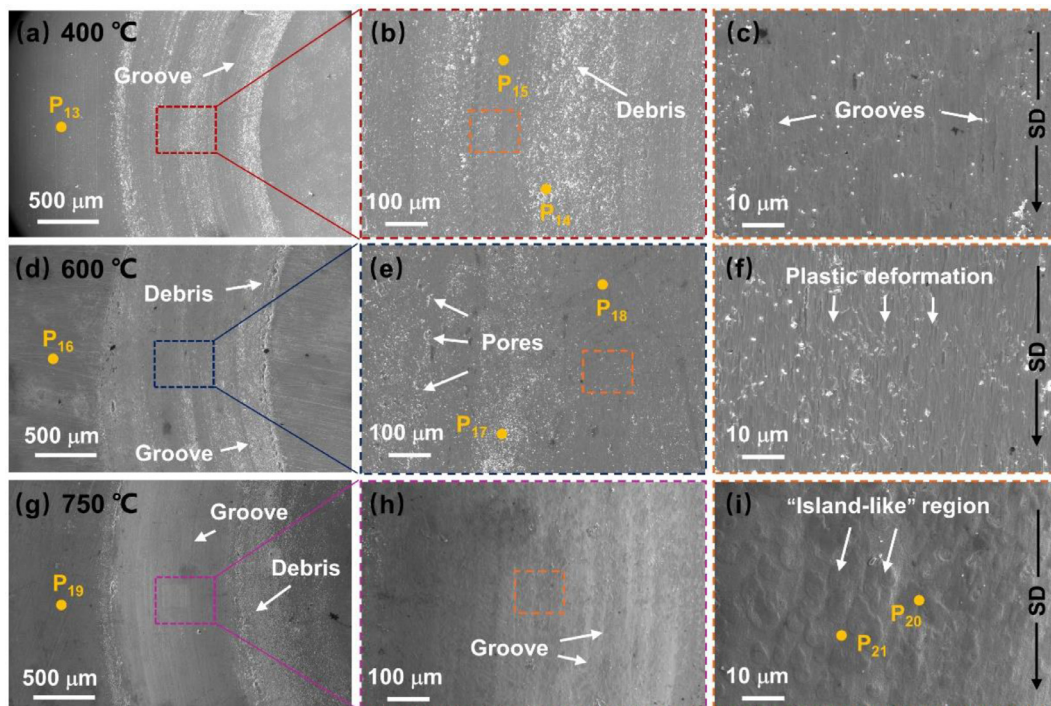


Fig. 7. (a–c) Wear morphology and elemental analysis of Ir-Ta-Ni-Nb BMG at 400 °C. (d–f) Wear morphology and elemental analysis of Ir-Ta-Ni-Nb BMG at 600 °C. (g–i) Wear morphology and elemental analysis of Ir-Ta-Ni-Nb BMG at 750 °C.

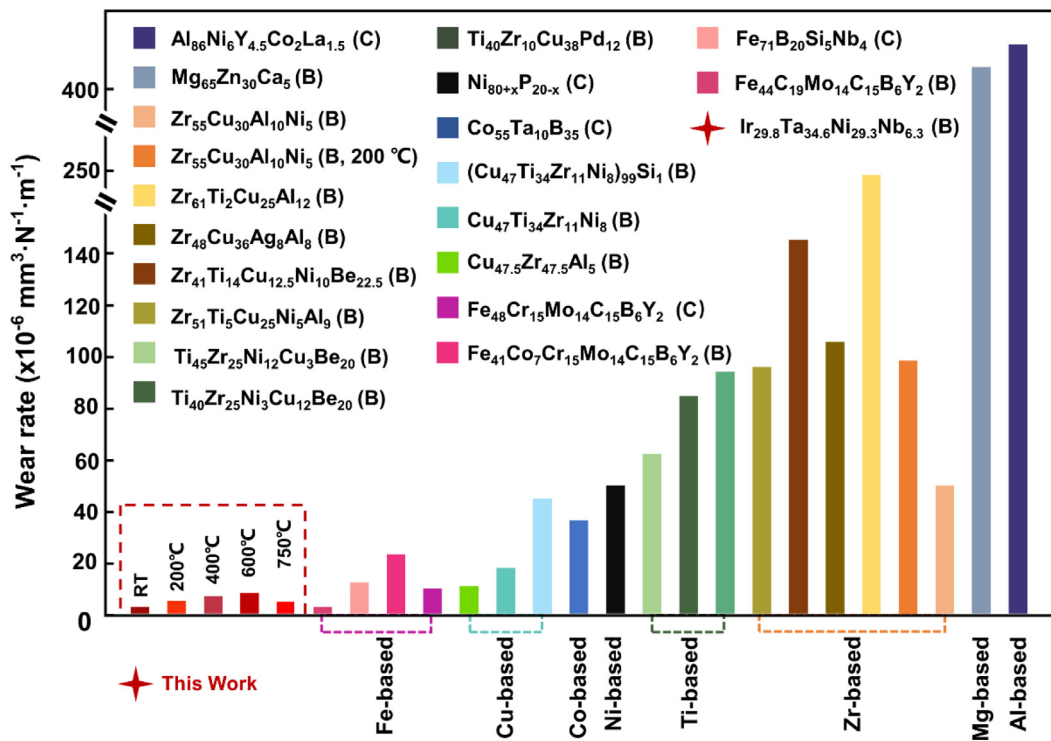


Fig. 8. Summary of wear rates for various MG systems.

can be observed, indicating the occurrence of abrasive wear and adhesive wear. In the magnified view (Fig. 7(b)), numerous oxide particles are found but no cracks or holes are observed. However, in the larger magnification image (Fig. 7(c)), small holes can be found, implying slight fatigue wear. The elemental distribution of non-wear zones (P₁₃), oxide particles (P₁₄), and grooves (P₁₅) is summarized in Table 3. The oxygen content in the non-wear

zone is 18.68%, which means that the Ta-based BMG is slightly oxidized at 400 °C. The oxygen content of the oxide particles and grooves is 53.20% and 23.77%, respectively, which implies the occurrence of oxidative wear. Therefore, the wear mechanisms of Ir_{29.8}Ta_{34.6}Ni_{29.3}Nb_{6.3} BMG at 400 °C are mainly oxidative wear, adhesive wear, and minor abrasive and fatigue wear. The low magnification SEM morphology (Fig. 7(d)) of the wear trace at 600 °C is

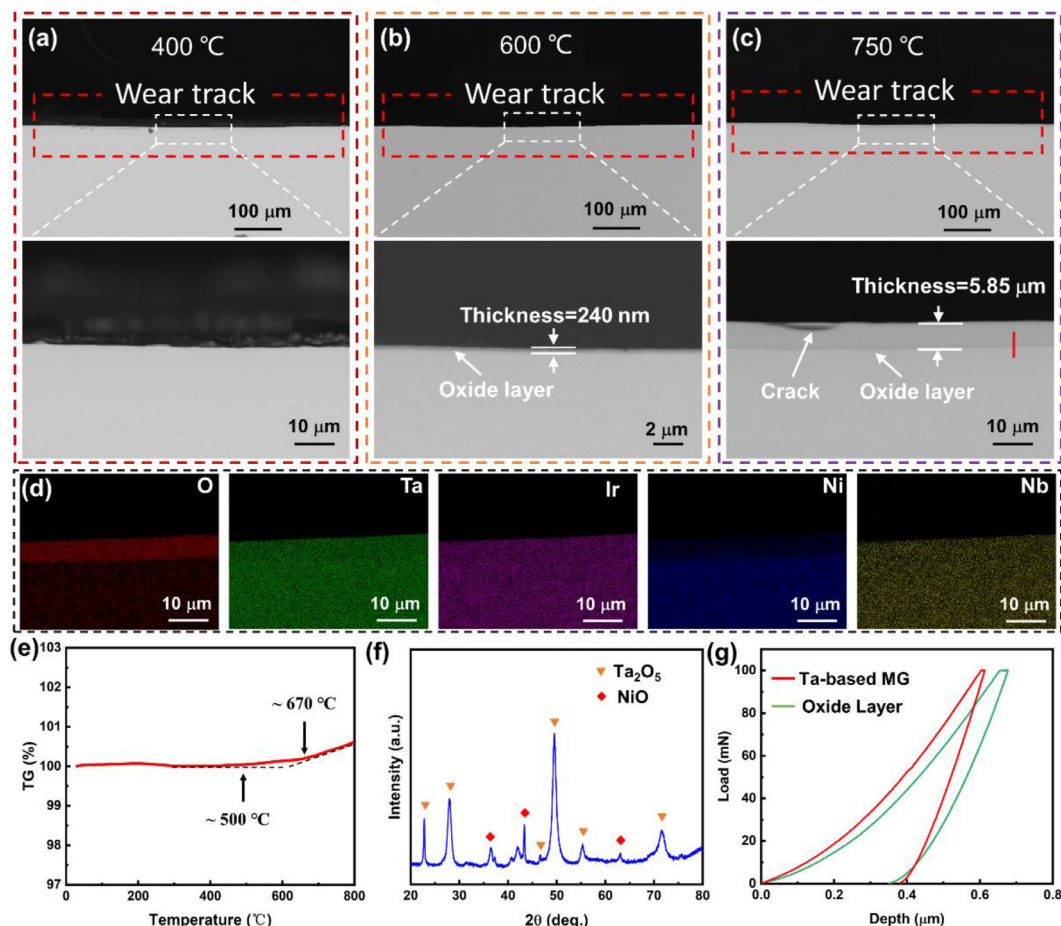


Fig. 9. (a–c) Backscattering morphology of the cross sections at 400 °C, 600 °C, and 750 °C. (d) Mapping analysis of the contrast difference layer. (e) Result of the weight increase of BMG in the air as a function of temperature. (f) Oxidation products of the surface analyzed using XRD. (g) Comparison of nanoindentation results of the BMG and oxide layer.

Table 3

Summary of the elemental distribution of Ir-Ta-Ni-Nb BMG at 400 °C, 600 °C, and 750 °C.

Point No.	Element Content (at.%)					
	Ir	Ta	Ni	Nb	Zr	O
P ₁₃	25.99	26.50	25.32	3.51	0.00	18.68
P ₁₄	15.03	14.90	14.51	2.36	0.00	53.20
P ₁₅	24.46	39.76	23.37	3.34	0.00	23.77
P ₁₆	14.95	15.20	16.10	1.63	0.00	52.12
P ₁₇	13.59	15.34	13.39	2.02	0.00	55.66
P ₁₈	15.79	15.62	14.04	2.13	0.00	52.41
P ₁₉	4.84	24.04	31.93	0.46	0.00	56.52
P ₂₀	9.76	10.32	13.89	1.24	0.00	64.84
P ₂₁	13.04	13.09	10.43	1.70	0.00	61.74

similar to that at 400 °C, where oxide particles and slight grooves can be observed. Fig. 7(e) shows an enlargement of a typical area in Fig. 7(d), and a small number of holes can be observed, implying the occurrence of fatigue wear. More details are captured in the enlarged view (Fig. 7(e)), and remarkably plastic deformation can be found on the surface of the wear trace, which indicates that the heat generated by friction further increases the temperature of the surface to reach the SLR of Ir_{29.8}Ta_{34.6}Ni_{29.3}Nb_{6.3} BMG. Similarly, the distribution of elements in different regions, including non-wear region (P₁₆), oxide particles (P₁₇), and groove (P₁₈), is summarized in Table 3. The oxygen content in the above three

regions exceeds 50%, which indicates that the ambient temperature of 600 °C leads to the oxidation of BMG. Therefore, the wear mechanism of Ir_{29.8}Ta_{34.6}Ni_{29.3}Nb_{6.3} BMG at 600 °C is oxidative wear, abrasive wear, and slight fatigue wear. The SEM morphology of the wear trace after wear at 750 °C is shown in Fig. 7(g), where slight grooves and numerous oxide particles can be found. Interestingly, the magnified views (Figs. 7(h, i)) show a distinctly different morphology from that at 400 °C and 600 °C. Distributed unique “island-like” features are observed on the surface of wear traces rather than oxide particles. The unique morphology implies a transformation of the primary wear mechanism at 750 °C, and the uneven “island-like” structure is the origin of the gradual upward trend of COF in Fig. 6(g). Correspondingly, the distribution of elements in the non-wear region (P₁₉) as well as inside and outside (P₂₀, P₂₁) of the island is summarized in Table 3. A further increase in the oxygen content is observed in all three regions, even exceeding 60% in the “island-like” region, which indicates that oxidative wear dominates the wear at 750 °C.

The specific wear rate ω is used to evaluate the wear resistance of the novel Ir_{29.8}Ta_{34.6}Ni_{29.3}Nb_{6.3} BMG, which is in accordance with Eq. (1). The wear results of Ir-Ta-Ni-Nb BMG at RT, 200 °C, 400 °C, 600 °C, and 750 °C, including wear volume (V_{loss}), wear rate (ω), and maximum wear depth (d_{max}) are summarized in Table 4. For comparison, the wear rates of various typical systems of BMG from literature, including Fe- [21,22,36,37], Cu- [24,38], Co- [27], Ni- [34], Ti- [20,24,39], Zr- [20,38,40,41], Mg- [25], and Al-based MG [23], at RT are tabulated in Table S1. The visual

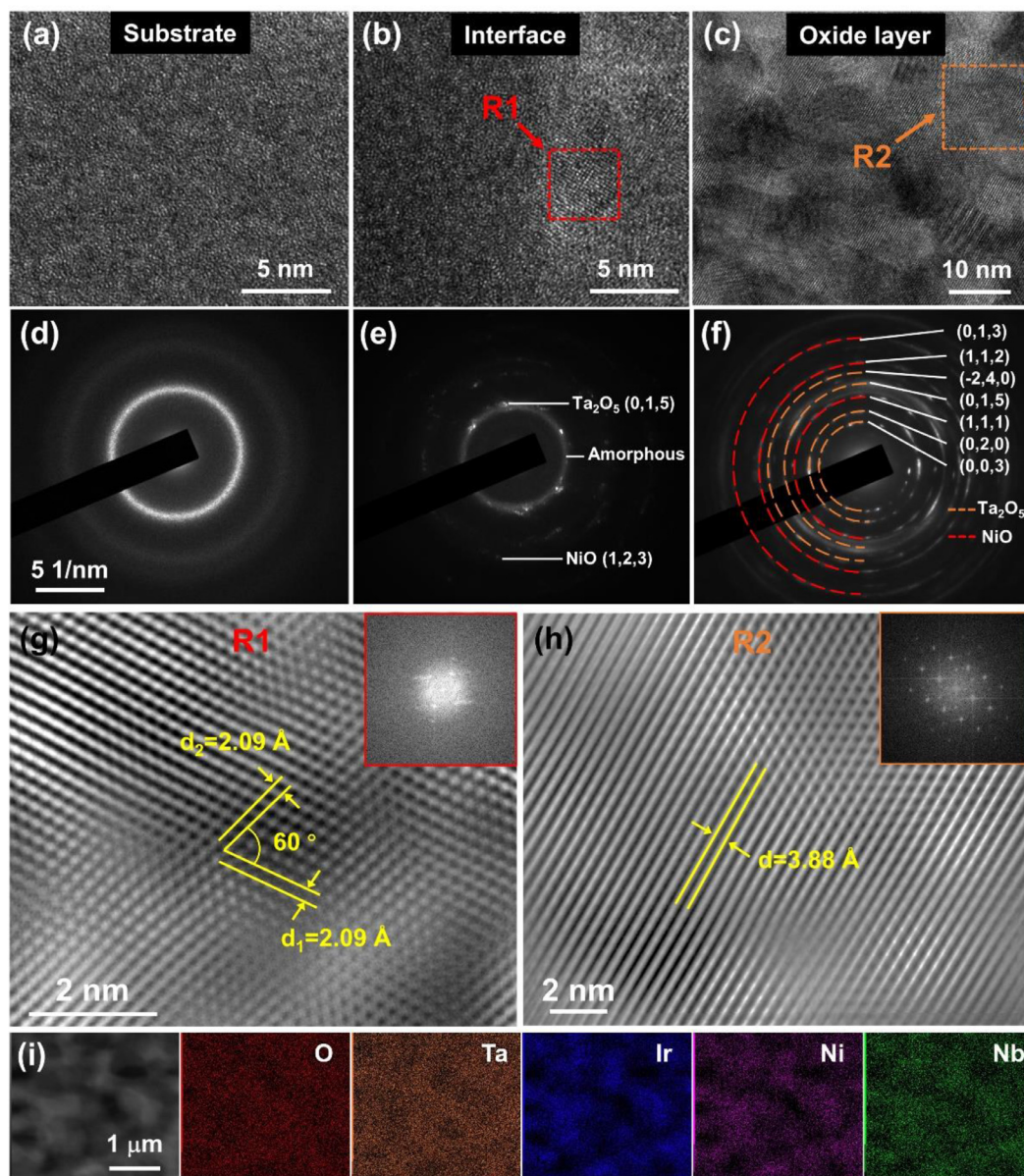


Fig. 10. (a–c) High-resolution images of three typical areas (BMG substrate, interface, and oxide layer, respectively) observed by HRTEM. (d–f) SAED images of three selected regions. (g) FFT and IFFT images of the marked region in Fig. 10(b). (h) FFT and IFFT images of the marked region in Fig. 10(c). (i) Typical HAADF-STEM image and the corresponding EDS elemental maps of the oxide layer.

Table 4
Summary of the wear results of Ir-Ta-Ni-Nb BMG.

Temperature (°C)	d_{\max} (m)	V_{loss} (m ³)	Wear rate ($\times 10^{-6}$ mm ³ N ⁻¹ m ⁻¹)
RT	2.1	358	2.65
200	2.9	1015	7.52
400	4.1	1429	10.59
600	5.0	2833	20.99
750	4.2	956	7.08

mapping of wear rate based on typical MG systems, including bulk (B) and coating (C), is plotted in Fig. 8 to facilitate the comparison. The Ir-Ta-Ni-Nb BMG exhibits comprehensive and superior wear resistance properties compared with other MG systems. Although Fe-based MG achieves near-wear resistance at RT, the Ir-Ta-Ni-Nb MG retains excellent resistance to wear at temperatures up to 750 °C, which is unachievable for the existing MG systems.

4. Discussion

4.1. Structure and composition of the oxide layer

To understand the enhancement of wear resistance of Ir_{29.8}Ta_{34.6}Ni_{29.3}Nb_{6.3} BMG at 750 °C, the cross-sectional morphology of the wear trace was observed by using the backscattering mode. The results after wear experiments at 400 °C, 600 °C, and 750 °C are presented in Fig. 9(a–c), respectively. It can be found that the cross-section at 400 °C exhibited a homogeneous contrast (see Fig. 9(a)), whereas a contrast difference of about 240 nm in thickness was observed at 600 °C (Fig. 9(b)). However, a contrast difference layer with a thickness of about 5.85 μm was detected on the cross-sectional morphology after wearing at 750 °C, as shown in Fig. 9(c). Cracks were observed in the results at 750 °C, which implies the occurrence of fatigue wear. By contrast, no visible cracks or holes were found in the cross-section after wearing at 400 °C and 600 °C, which indicates that no serious fatigue wear

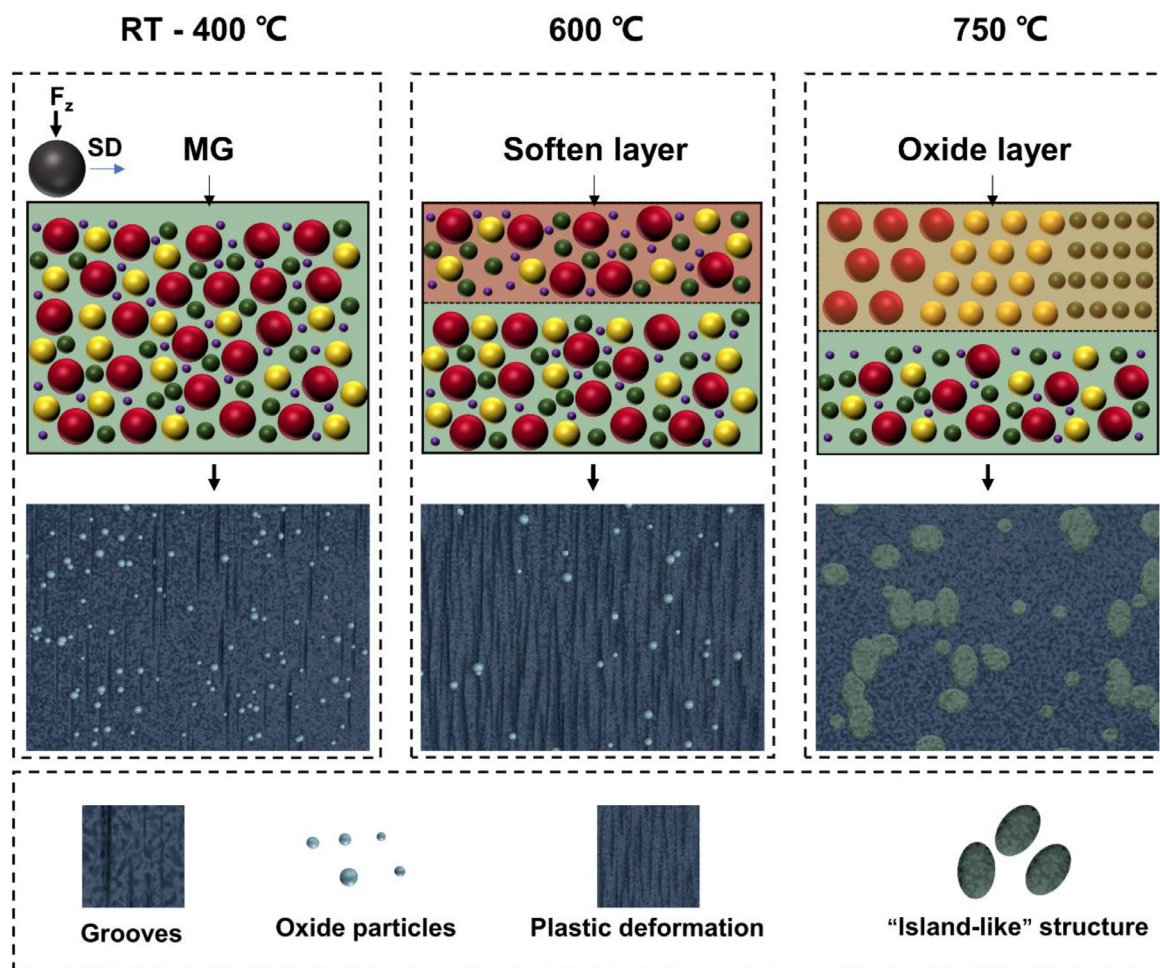


Fig. 11. Diagram of the wear mechanism at different temperatures.

occurred. The distribution of elements in this region was analyzed by using EDS to confirm the origin of the contrast difference layer. As presented in Fig. 9(d), the contrast difference layer reveals an oxygen enrichment, which indicates the formation of a thicker oxide layer on the surface of Ir-Ta-Ni-Nb BMG at 750 °C. It is consistent with the results of increasing weight as a function of temperature in air tested using a thermogravimetric analyzer. As shown in Fig. 9(e), the Ir-Ta-Ni-Nb BMG starts to gain weight at ~500 °C, and the rate of weight gain increases remarkably at ~670 °C. The different oxidation rates lead to the generation of oxide layers with different thicknesses, and the oxide layer generated at 750 °C dominates the wear process rather than the MG substrate. The oxidation products on the surface were identified using XRD, and the results revealed that the oxide layer is mainly composed of Ta₂O₅ and NiO, which is in agreement with the reported Ir-Ta-Ni-(B) BMG system [30]. The hardness and modulus of the Ir-Ta-Ni-Nb BMG and oxide layer were determined by nanoindentation using a peak load of 100 mN. The corresponding load vs displacement curves are shown in Fig. 9(g). The data were averaged after collecting 10 points for every sample to ensure accuracy. The average hardness and modulus of the original BMG can be calculated as 13.9 and 191.5 GPa, while the average hardness and modulus of the oxide layer are 11.9 and 151.4 GPa, respectively.

The structures and compositions of the samples after the 750 °C wear test was further analyzed by using cross-sectional TEM. Fig. 10(a–c) shows the high-resolution structures at the combination area (BMG substrate, interface, and oxide layer, respectively) observed by high-resolution TEM (HRTEM). The three regions show

different atomic structures, the BMG substrate is a typical amorphous structure, the interface region is a combination of ordered and disordered structures, and the oxidation region is a typical crystalline structure. Accordingly, the above three regions were chosen for selected area electron diffraction (SAED). The results are shown in Fig. 10(d–f), respectively. The diffraction pattern corresponding to the BMG substrate shows a pure diffraction ring, which indicates that the amorphous nature is maintained even after the 750 °C wear test. The region corresponding to the interface shows a combination of crystal spots, and a halo ring shows a typical crystalline state. The region corresponding to the oxide layer shows a pronounced crystal structure and can be identified as Ta₂O₅ and NiO, which is consistent with the XRD results (Fig. 9(f)). The fast Fourier transform (FFT) and inverse FFT (IFFT) images for a typical region (marked as R1) of Fig. 10(b) are shown in Fig. 10(g) and its inset, respectively. The 2.09 Å spaced lattice fringes of the crystal phases in Fig. 10(g) could correspond to the (200) plane of NiO. Similarly, the FFT and IFFT images for a typical region (marked as R2) of Fig. 10(c) are shown in Fig. 10(h) and its inset, respectively. The 3.08 Å spaced lattice fringes of the crystal phases in Fig. 10(h) correspond to the (210) plane of Ta₂O₅. A representative area was selected for high-resolution TEM coupled with EDS analysis to reveal more detailed chemical and structural information for the oxide layer (Fig. 10(i)). The EDS results indicate the richness of Ta and O elements, and the bias of Ir, Ni, and Nb elements, which further proves the main composition of the oxidation products. When the ambient temperature of wear is set to 750 °C, the Ta-based MG underwent intense oxidation in accordance with

the results of Fig. 9(c–e). Therefore, the actual wear involved at this point is an oxide layer of several microns in thickness.

4.2. Wear mechanisms at variable temperatures

The Ir_{29.8}Ta_{34.6}Ni_{29.3}Nb_{6.3} BMG demonstrates a superior high-temperature wear resistance, following different wear mechanisms at various ambient temperatures. To facilitate understanding, we illustrated the wear mechanism of Ir-Ta-Ni-Nb BMG at different temperatures based on the previous results. As shown in Fig. 11, the warming caused by frictional heat is insufficient to soften the surface due to the ultrahigh T_g temperature (~ 827 °C) of the Ta-based MG at RT–400 °C, and the actual wear involved is the rigid MG substrate with disordered atomic structure. The wear behavior at this point is mainly dominated by the hardness, and the worn surface mainly shows minor grooves caused by abrasive wear and the distribution of oxide particles due to frictional flash temperature due to the high hardness (~ 13.9 GPa) of the Ir-Ta-Ni-Nb MG (Fig. 5(a) and Fig. 7(a)). When the temperature is set to 600 °C, the heating up caused by frictional heat reaches the SLR of Ta-based BMG. In this case, the softening layer of MG is involved in the wear, and the wear is the most intense with a wear rate of $20.99 \times 10^{-6} \text{ mm}^3 \text{ N}^{-1} \text{ m}^{-1}$ (Fig. 6(d–f)). The wear surface is characterized by intense plastic deformation and the distribution of oxide particles due to frictional flash temperature (see Fig. 7(e, f)). Given that the hardness of the oxide layer (~ 11.9 GPa) is lower than that of the Ta-based BMG at RT, the wear rate at 750 °C ($\sim 7.08 \times 10^{-6} \text{ mm}^3 \text{ N}^{-1} \text{ m}^{-1}$) is higher than that at RT ($\sim 2.65 \times 10^{-6} \text{ mm}^3 \text{ N}^{-1} \text{ m}^{-1}$) but lower than that of the softened BMG layer at 600 °C ($\sim 20.99 \times 10^{-6} \text{ mm}^3 \text{ N}^{-1} \text{ m}^{-1}$), as summarized in Table 4 and Fig. 8. Owing to the intense oxidation, the wear surface consists of a large number of “island-like” oxidation products (corresponding to Fig. 7(h, i)), and this convex structure leads to the gradual increase in COF (Fig. 6(g)).

5. Conclusions

In this study, the wear behaviors and mechanisms of a novel Ta-based BMG at RT and elevated temperatures were investigated in depth. At relatively low temperatures from RT to 400 °C, the wear behavior is mainly influenced by hardness, and the wear mechanisms are mainly minor abrasive wear and oxidative wear due to flash temperatures during friction. The corresponding wear rates at RT, 200 °C, and 400 °C are $2.65 \times 10^{-6} \text{ mm}^3 \text{ N}^{-1} \text{ m}^{-1}$, $7.52 \times 10^{-6} \text{ mm}^3 \text{ N}^{-1} \text{ m}^{-1}$, and $10.59 \times 10^{-6} \text{ mm}^3 \text{ N}^{-1} \text{ m}^{-1}$, respectively. At a higher temperature of 600 °C, the further heating induced by frictional heat leads to softening of the BMG surface, which results in intense wear with a wear rate of $20.99 \times 10^{-6} \text{ mm}^3 \text{ N}^{-1} \text{ m}^{-1}$. The corresponding wear mechanisms are softness-driven abrasive wear and oxidative wear caused by flash temperatures during friction. At the highest temperature of 750 °C, the oxide layer with a thickness of several microns formed on the surface of Ta-based BMG undergoes the wear process instead of the substrate, showing enhanced wear resistance with a wear rate of $7.08 \times 10^{-6} \text{ mm}^3 \text{ N}^{-1} \text{ m}^{-1}$. In summary, we demonstrated the superior high-temperature wear resistance of Ir-Ta-Ni-Nb BMG, which elucidates its wide application in precision instruments and under extreme conditions.

Data availability

The data that support the findings of this study are available from the corresponding author upon reasonable request.

Declaration of competing interest

The authors declare that they have no known competing financial interests or personal relationships that could have appeared to influence the work reported in this paper.

CRediT authorship contribution statement

Fei Sun: Methodology, Validation, Formal analysis, Investigation, Data curation, Writing – original draft, Writing – review & editing, Visualization. **Shengtao Deng:** Investigation, Methodology, Validation. **Jianan Fu:** Methodology, Investigation. **Jiahua Zhu:** Writing – review & editing, Visualization. **Dandan Liang:** Investigation, Supervision. **Pengfei Wang:** Investigation, Supervision. **Hang Zhao:** Investigation, Supervision. **Feng Gong:** Investigation, Supervision. **Jiang Ma:** Investigation, Writing – review & editing, Supervision. **Yanhui Liu:** Investigation, Writing – review & editing, Supervision. **Jun Shen:** Investigation, Writing – review & editing, Supervision.

Acknowledgements

The work was financially supported by the National Key Research and Development Program of China (Grant No. 2018YFA0703605), the Key Basic and Applied Research Program of Guangdong Province, China (Grant No. 2019B030302010), the NSF of China (Grant No. 52122105, 51971150), and the Science and Technology Innovation Commission Shenzhen (Grants No. RCJC20221008092730037, 20220804091920001). The authors also thank the assistance on microscope observation received from the Electron Microscope Center of Shenzhen University.

Supplementary materials

Supplementary material associated with this article can be found, in the online version, at doi:10.1016/j.jmst.2023.02.040.

References

- [1] T. Eyre, Tribol. Int. 9 (1976) 203–212.
- [2] J. Luo, W. Sun, D. Liang, K.C. Chan, X.S. Yang, F. Ren, Acta Mater. 243 (2023) 118503.
- [3] Q. Jia, W.H. He, D.P. Hua, Q. Zhou, Y. Du, Y. Ren, Z.B. Lu, H.F. Wang, F. Zhou, J. Wang, Acta Mater. 232 (2022) 117934.
- [4] P.K. Katiyar, Int. J. Refract. Met. Hard Mater. 92 (2020) 105315.
- [5] C. Schuh, T. Hufnagel, U. Ramamurty, Acta Mater. 55 (2007) 4067–4109.
- [6] I. Konyashin, B. Ries, D. Hlawatschek, Y. Zhuk, A. Mazilkin, B. Straumal, F. Dorn, D. Park, Int. J. Refract. Met. Hard Mater. 49 (2015) 203–211.
- [7] M. Moore, Wear 28 (1974) 59–68.
- [8] W. Klement, R.H. Willens, P. Dumez, D. Pol, Nature 187 (1960) 869–870.
- [9] A.L. Greer, Science 31 (1995) 1947–1953.
- [10] F. Sun, B. Wang, F. Luo, Y.Q. Yan, H.B. Ke, J. Ma, J. Shen, W.H. Wang, Mater. Des. 190 (2020) 108595.
- [11] C. Zhang, D. Ouyang, S. Pauly, L. Liu, Mater. Sci. Eng. R 145 (2021) 100625.
- [12] J. Schroers, JOM 57 (2005) 35–39.
- [13] J. Schroers, Adv. Mater. 22 (2010) 1566–1597.
- [14] G. Duan, A. Wiest, M.L. Lind, J. Li, W.K. Rhim, W.L. Johnson, Adv. Mater. (2007) 4272–4275.
- [15] J.Y. Zhang, Z.Q. Zhou, Z.B. Zhang, M.H. Park, Q. Yu, Z. Li, J. Ma, A.D. Wang, H.G. Huang, M. Song, B.S. Guo, Q. Wang, Y. Yang, Mater. Futures 1 (2022) 012001.
- [16] Y.H. Liu, G. Wang, R.J. Wang, D.Q. Zhao, M.X. Pan, W.H. Wang, Science 315 (2007) 1385–1388.
- [17] Z. Li, Z. Huang, F. Sun, X. Li, J. Ma, Mater. Today Adv. 7 (2020) 100077.
- [18] F. Sun, J. Yang, J.A. Fu, B. Wang, J. Ma, J. Shen, J. Non-Cryst. Solids 594 (2022) 121821.
- [19] G. Kumar, H.X. Tang, J. Schroers, Nature 457 (2009) 868–872.
- [20] Y. Sun, Y.J. Huang, H.B. Fan, F.Y. Liu, J. Shen, J.F. Sun, J.J. Chen, J. Non-Cryst. Solids 406 (2014) 144–150.
- [21] Y.C. Li, C. Zhang, W. Xing, S.F. Guo, L. Liu, ACS Appl. Mater. Interface 10 (2018) 43144–43155.
- [22] N.B. Hua, X.N. Zhang, Z.L. Liao, X.S. Hong, Q.H. Guo, Y.T. Huang, X.Y. Ye, W.Z. Chen, T. Zhang, X.Q. Jin, Q.T. Wang, P.K. Liaw, J. Non-Cryst. Solids 543 (2020) 120065.

- [23] M.H. Gao, W.Y. Lu, B.J. Yang, S.D. Zhang, J.Q. Wang, *J. Alloy. Compd.* 735 (2018) 1363–1373.
- [24] M.L. Rahaman, L.C. Zhang, M. Liu, W.D. Liu, *Wear* 332–333 (2015) 1231–1237.
- [25] N.B. Hua, W.Z. Chen, Q.T. Wang, Q.H. Guo, Y.T. Huang, T. Zhang, *J. Alloy. Compd.* 745 (2018) 111–120.
- [26] N.B. Hua, W.Z. Chen, W.G. Wang, H.T. Lu, X.Y. Ye, G.H. Li, C. Lin, X.F. Huang, *Mater. Sci. Eng. C* 66 (2016) 268–277.
- [27] X.B. Liu, J.Z. Bi, Z.Y. Meng, R. Li, Y. Li, T. Zhang, *Tribol. Int.* 162 (2021) 107142.
- [28] H. Wu, I. Baker, Y. Liu, X. Wu, P.R. Munroe, J. Zhang, *Intermetallics* 35 (2013) 25–32.
- [29] C. Zhang, L. Liu, K.C. Chan, Q. Chen, C.Y. Tang, *Intermetallics* 29 (2012) 80–85.
- [30] M.X. Li, S.F. Zhao, Z. Lu, A. Hirata, P. Wen, H.Y. Bai, M. Chen, J. Schroers, Y. Liu, W.H. Wang, *Nature* 569 (2019) 99–103.
- [31] A. Inoue, T. Zhang, *Mater. Trans. JIM* 37 (1996) 185–187.
- [32] Y. Jiang, Z.M. Xie, J.F. Yang, Q.F. Fang, *Int. J. Refract. Met. Hard Mater.* 84 (2019) 104992.
- [33] N.B. Hua, Z.L. Zheng, H. Fang, X.Y. Ye, C. Lin, G.H. Li, W.G. Wang, W.Z. Chen, T. Zhang, *J. Non-Cryst. Solids* 426 (2015) 63–71.
- [34] M. Pole, M. Sadeghilaridjani, J. Shittu, C. Mahajan, N. Ghodki, S. Mukherjee, *Mater. Sci. Eng. A* 816 (2021) 141315.
- [35] S. Bajpai, A. Nisar, R.K. Sharma, U.D. Schwarz, K. Balani, A. Datye, *Wear* 486–487 (2021) 204075.
- [36] B. Sun, J.B. Cheng, Z.H. Cai, H.C. Zhao, Z.B. Zhang, H.Q. Qu, Q. Zhang, S. Hong, X.B. Liang, *Surf. Coat. Technol.* 405 (2021) 126598.
- [37] J.J. Xu, J.J. Kang, W. Yue, Z.Q. Fu, L.N. Zhu, D.S. She, *J. Non-Cryst. Solids* 573 (2021) 121136.
- [38] J. Kong, D.S. Xiong, J.L. Li, Q.X. Yuan, R. Tyagi, *Tribol. Lett.* 35 (2009) 151–158.
- [39] B.Z. Lin, K.H. Yang, X.G. Bao, J.L. Liu, Q.H. Guo, L. Zhang, Q.T. Wang, N.B. Hua, *J. Non-Cryst. Solids* 576 (2022) 121231.
- [40] X.F. Jiang, J.J. Song, Y.F. Su, H.Z. Fan, Y.S. Zhang, L.T. Hu, *Tribol. Int.* 136 (2019) 395–403.
- [41] Y. Wang, L.L. Shi, D.L. Duan, S. Li, J. Xu, *Mater. Sci. Eng. C* 37 (2014) 292–304.